Nature Communications

https://doi.org/10.1038/s41467-026-69635-2

Article in Press

A unified symmetry framework for spin–ferroelectric coupling in altermagnetic multiferroics

Received: 6 November 2025

Accepted: 5 February 2026

Cite this article as: Sun, W., Wang, W., Yang, C. *et al.* A unified symmetry framework for spin–ferroelectric coupling in altermagnetic multiferroics. *Nat Commun* (2026). https://doi.org/10.1038/s41467-026-69635-2

Wei Sun, Wenxuan Wang, Changhong Yang, Shifeng Huang & Zhenxiang Cheng

A unified Symmetry Framework for Spin – Ferroelectric Coupling in Altermagnetic Multiferroics

Wei Sun[1], Wenxuan Wang[2]*, Changhong Yang[1], Shifeng Huang[1]*, Zhenxiang Cheng[3]*

1 Shandong Provincial Key Laboratory of Green and Intelligent Building Materials, University of Jinan, Jinan, 250022, China

2 School of Material Science and Engineering, University of Jinan, Jinan, 250022, Shandong, China

3 Institute for Superconducting & Electronic Materials, Faculty of Engineering and Information Sciences, University of Wollongong, Innovation Campus, Squires Way, North Wollongong, NSW 2500, Australia

* Corresponding Author:

Wenxuan Wang, E-mail: mse_wangwx@ujn.edu.cn

Shifeng Huang, E-mail: mse_huangsf@ujn.edu.cn

Zhenxiang Cheng, E-mail: cheng@uow.edu.au

ABSTRACT

Altermagnetic multiferroics, hosting coexisting spin-splitting bands and ferroelectric polarization, offer a promising route to magnetoelectric coupling beyond conventional relativistic spin–orbit mechanism. However, the lack of a unified principle connecting ferroelectric switching symmetry to spin-band topology has impeded rational material design. Here, we establish a universal symmetry-based framework that classifies all possible spin–ferroelectric couplings in altermagnets into three fundamental types: decoupling, pseudo-time-reversal coupling, and asymmetric momentum mapping. This classification stems directly from the relation between ferroelectric switching operators and the spin Laue group, creating a decisive symmetry-to-function paradigm. First-principles calculations on bilayer $MnPS_3$ confirm the framework, showing that distinct ferroelectric switching paths produce characteristic spin-band reconstructions and discriminable

electrical transport signatures. The universality of the framework is further validated in $BiFeO_3$. Our work provides a predictive design principle for voltage-programmable spintronics, effectively transforming ferroelectric symmetry from a structural descriptor into a dynamic functional control knob for altermagnetic spin states.

I. INTRODUCTION

Altermagnetic multiferroics—materials that simultaneously host altermagnetic and ferroelectric orders—represent a new frontier in the design of strongly coupled magnetoelectric systems.[1-4] Conventional multiferroics are often limited by the inherent separation between the coexisting ferroelectric and magnetic orders, resulting in weak magnetoelectric coupling that typically depends on spin-orbit coupling (SOC) as an indirect mediator.[5,6] In contrast, altermagnetic multiferroics feature opposite spin sublattices within the crystal lattice, which are connected by rotation or mirror symmetries, while prohibiting connection through translational or inversion symmetries.[7-15] This gives rise to momentum-space spin splitting in the compensated magnetic ordering, which is naturally compatible with the inversion symmetry breaking induced by the ferroelectric. Central to this is the spatial symmetry, which serves as a key parameter for geometrically coupling the spin-split electronic bands of altermagnets with the switchable ferroelectric polarization, bypassing the reliance on SOC. This intrinsic symmetry coupling offers a direct route to achieving robust magnetoelectric responses, fulfilling the critical requirements for next-generation spintronic memory and logic devices.[16-27]

Recent theoretical studies have shown that in various low-dimensional and three-dimensional altermagnetic multiferroic materials, ferroelectric switching can reversibly modulate the spin texture without altering the global magnetic ordering.[28-32] This offers an ideal platform for electric-field control of spin states and highlights promising prospects for low-power, nonvolatile spintronic applications. However, it is important to note that this coupling is subject to strict symmetry constraints. For example, in some altermagnetic multiferroics, it has been found that the switching of ferroelectric polarization does not affect the spin electronic bands of the

altermagnetic.[29,31] This suggests that the coexistence of ferroelectric and altermagnetic does not necessarily lead to their coupling, and the symmetry conditions that govern whether such coupling occurs remain unclear. More fundamentally, a unified theoretical framework is still lacking to systematically describe how ferroelectric switching modulates altermagnetic spin splitting. In particular, symmetry-based classification criteria that can predict spin responses under different switching operations remain underdeveloped, hindering rational material design and functional optimization.

To address this gap, we develop a group-theoretic classification of spin–ferroelectric coupling in altermagnets. Our analysis identifies three fundamental response types—Type I: spin–ferroelectric decoupling, and Type II: pseudo-time-reversal (pseudo-spin-flip) coupling, and Type III: non-symmetric momentum mapping—each determined by the relationship between the ferroelectric switching operator and the crystal's spin Laue group. These theoretical predictions are first confirmed through first-principles calculations on bilayer $MnPS_3$ and subsequently validated in $BiFeO_3$ as a prototypical 3D system, in which distinct ferroelectric switching paths are shown to produce characteristic spin-band reconstructions.

This work establishes a unified symmetry-guided framework for understanding and designing altermagnetic multiferroics with tailored magnetoelectric functionality. The distinct spin-band reconstructions further give rise to discriminable electrical transport signatures, enabling simple electrical measurements to serve as direct experimental fingerprints of the three symmetry-determined coupling types. Thus, the framework not only offers fundamental theoretical insight but also provides a practical material platform for the development of voltage-programmable, low-power spintronic devices.

II. RESULTS

1. Group-Theoretical Analysis of Spin–Ferroelectric Locking

In crystals, symmetry imposes fundamental constraints on the electronic band structure. For any non-relativistic spin space operation $\widehat{U} = [g_s||g_r]$, the crystal Hamiltonian obeys the

conjugation relation $\hat{U}H(\mathbf{k})\hat{U}^{-1} = H(\mathbf{k}')$. Consequently, the energy eigenvalues transform as:

$$\hat{U}E(\mathrm{s},\mathbf{k}) = [g_s||g_r]E(\mathrm{s},\mathbf{k}) = E(s',\mathbf{k}') \quad (1)$$

Where, g_s (g_r) acts in spin (real) space, with $s' = g_s s$ and $\mathbf{k}' = g_r\mathbf{k}$. In conventional ferromagnetic or antiferromagnetic systems, this relation ensures common features such as spin splitting or degeneracy. In non-relativistic altermagnets, however, specific spatial operations exchange opposite-spin sublattices, corresponding to a nontrivial spin Laue group[7]:

$$R_{\mathrm{AM}} = [E||\mathbf{H}] + [C_2||A][E||\mathbf{H}] = [E||\mathbf{H}] + [C_2||\mathbf{G}-\mathbf{H}] \quad (2)$$

Here, $\mathbf{H} \subset \mathbf{G}$ is a halving subgroup of the crystallographic Laue group, representing operations that preserve the same spin sublattice. The coset $\mathbf{G} - \mathbf{H} = A\mathbf{H}$ is generated by an element A, which is a real-space rotation or mirroring (excluding pure inversion or translation; hence, the inversion operation in **G** is contained within **H**). The action of A connects the two opposite-spin sublattices. Thus, the band structure of an altermagnet satisfies:

$$E(s,\mathbf{k}) = [E||\mathbf{H}]E(s,\mathbf{k}) = E(s,\mathbf{H}\mathbf{k}) \quad (3)$$

$$E(s,\mathbf{k}) = [C_2||A\mathbf{H}]E(s,\mathbf{k}) = E(-s,A\mathbf{k}) \quad (4)$$

In this formulation, **H** ensures $\mathbf{k} = h\mathbf{k}$ for all $h \in \mathbf{H}$, whereas for $\mathbf{k} \neq A\mathbf{k}$, the relations correspond to an alternating sign pattern of spin splitting in momentum space.

Furthermore, non-relativistic collinear magnets possess a fundamental symmetry $[\bar{C}_2||T]$, which implies:

$$E(s,\mathbf{k}) = [\bar{C}_2||T]E(s,\mathbf{k}) = E(s,-\mathbf{k}) = [E||I]E(s,\mathbf{k}) \quad (5)$$

This indicates that the band structure always preserves inversion symmetry I in momentum space (**k** = -**k**), even if the crystal lacks real-space inversion symmetry.

We now consider the ferroelectric switching operation O_{FE} acting in real space, represented as a symmetry operation $\hat{U} = [E||O_{\mathrm{FE}}]$, which reverses the ferroelectric polarization **P** while preserving the system's magnetic configuration, i.e., $[E||O_{FE}]\mathbf{P} = \mathbf{P}'$. Note that the operation $\hat{U}$ is independent of its own symmetry; rather, it describes a transformation that maps one system to another with different polarization. During this process, the spins remain unchanged in real space, but exhibit distinct responses in momentum space. By matching the real-space ferroelectric

switching operation with the Laue group in momentum space, three distinct types of effects on the spin-resolved band structure $E(s, \mathbf{k})$ of an altermagnet are observed, as illustrated in Fig. 1.

(1) Type I: Spin-ferroelectric decoupling described by $O_{FE} \in \mathbf{H}$

$$[E||O_{FE}]E(s,\mathbf{k}) = E(s, O_{FE}\mathbf{k}) = E(s,\mathbf{k}) \tag{6}$$

Here, the energy eigenvalues for each spin channel remain unchanged at all **k**-points. Ferroelectric switching in this case leaves the spin-split spectrum unmodified, representing a decoupled regime with no direct spectral signature.

(2) Type II: Pseudo-time-reversal coupling described by $O_{\mathrm{FE}} \in A\mathbf{H}$

Since **H** is a halving subgroup of **G** and the generator A satisfies $A^2 \in \boldsymbol{H}$, it follows that $A\mathbf{H} = A^{-1}\mathbf{H}$. Thus, the action of ferroelectric switching in momentum space satisfies $O_{\mathrm{FE}}\mathbf{k} = A^{-1}\mathbf{k}$, and the corresponding energy eigenvalue mapping becomes:

$$[E||O_{FE}]E(s,\mathbf{k}) = [E||O_{FE}][C_2||A\mathbf{H}]E(s,\mathbf{k}) = E(-s,\mathbf{k}) = E(-s,-\mathbf{k}) \tag{7}$$

This operation effectively flips the spin label, acting as a pseudo-time-reversal (or pseudo-spin-flip). Ferroelectric switching thus induces a global spin spectrum reversal, representing strong spin–ferroelectric coupling.

(3) Type III: General non-symmetric mapping described by $O_{FE} \notin \mathbf{G}$

$$[\mathrm{E}||O_{FE}]\mathrm{E}(\mathrm{s},\mathbf{k}) = \mathrm{E}(\mathrm{s}, O_{FE}\mathbf{k}), \qquad \mathbf{k} \neq O_{FE}\mathbf{k} \tag{8}$$

In this case, ferroelectric switching does not correspond to any symmetry element that preserves or exchanges spin sublattices. Instead, it geometrically maps the spin texture in momentum space, leading to momentum-dependent spin reconstructions and an anisotropic response that varies across the Brillouin zone.

In summary, the effect of ferroelectric switching on spin is classified as:

$$[E||O_{FE}]E(s,\mathbf{k}) = \begin{cases} E(s,\mathbf{k}), & O_{FE} \in \mathbf{H} \quad (\text{Type I}) \\ E(-s,\mathbf{k}), & O_{FE} \in A\mathbf{H} \quad (\text{Type II}) \\ E(s, O_{FE}\mathbf{k}), & O_{FE} \notin \mathbf{G} \quad (\text{Type III}) \end{cases} \tag{9}$$

We further obtained numerical results from the tight-binding model constructed under the *2*/*m* Laue group (Fig. S1), which are in perfect agreement with the aforementioned group-theoretical classification. This further validates the impact of different ferroelectric switching symmetries on the three characteristic types of spin bands in altermagnetism.

Notably, in altermagnets, the set $\{E, I\}$ always belong to **H**. Thus, any ferroelectric switching operation involving only inversion leaves the spin spectrum unaffected and is inherently of Type I. This is particularly relevant in 2D systems, where the *z*-component is a pseudoscalar, rendering the set $\{C_{2z}, M_z\}$ effectively equivalent to $\{E, I\}$. Therefore, operations $O_{\mathrm{FE}} \in \{I, C_{2z}, M_z\}$ in 2D systems are invariably classified as Type I, remaining decoupled from spin in any Laue group.

2. First-Principles Validation in 2D bilayer $MnPS_3$

First-principles calculations offer a realistic platform for validating the theoretical classification of spin–ferroelectric locking. We selected bilayer $MnPS_3$ as a candidate system, where sliding ferroelectricity in van der Waals bilayers exhibit exceptional tunability. Unlike conventional ferroelectrics with a single, fixed switching path, polarization reversal in this system can be realized through multiple layer-sliding trajectories defined by distinct symmetry operations. This intrinsic flexibility makes sliding ferroelectrics an ideal platform for systematically exploring different ferroelectric switching symmetries within a single material family.

Starting from a monolayer of $MnPS_3$ with Néel-type antiferromagnetic ordering (its relevant structural and magnetic properties are presented in Fig. S2), we construct the bilayer by applying the mapping $\{M_z|\tau_o\}$ together with an out-of-plane translation τ_z, resulting in a crystallographic point group of *m* and a crystallographic Laue group of *2/m*, with the full set of symmetry operations $\mathbf{G} = \{E, C_{2y}, I, M_y\}$. The halving subgroup $\mathbf{H} = \{E, I\}$ preserves each spin sublattice. Consequently, the system is governed by the altermagnetic group $R_{\mathrm{AM}} = [E||\{E, I\}] + [C_2||\{C_{2y}, M_y\}]$, which generates the characteristic alternating sign pattern of spin splitting in the Brillouin zone. In this construction, the sliding ferroelectric polarization **P** is controlled by the in-plane translation vector τ_o of the top layer relative to the bottom layer. DFT total-energy scans identify a global maximum

for the paraelectric phase at $\tau_0 = (0,0)$, along with six degenerate global minima for the ferroelectric phase at $\tau_0 \in \{(va,0), (0,vb), (va,vb) \mid v = \pm 1/3\}$, as shown in Fig. 2b, leading to uncompensated interfacial charge transfer and a combined polarization of 0.92 μC/m (in-plane) and 0.26 μC/m (out-of-plane), as demonstrated by the charge difference between the paraelectric and ferroelectric phases in Fig. S3. We identify three transition paths: path 1 maintains the crystal's mirror symmetry orientation and reverses only the out-of-plane component with an energy barrier of 11.8 meV/f.u., while paths 2 and 3 rotate the crystal's mirror symmetry orientation by π/3, switch both in-plane and out-of-plane components. The energy barriers for paths 2 and 3 are degenerate, both at 9.2 meV/f.u. (Fig. 2c). The theory of bilayer stacking ferroelectricity (BSF) provides a method for selectively choosing sliding paths using an external electric field,[33] allowing for controllable polarization switching, as shown in Fig. S4.

To comprehensively investigate possible ferroelectric switching symmetries in the system, we employ two distinct interlayer antiferromagnetic configurations as analysis platforms. The two configurations are nearly degenerate in energy (difference ~0.22 meV), indicating weak interlayer exchange coupling. For compact notation, we denote the polarization as $\mathbf{P}_n^{\pm}(\mathbf{L}_m)$, where the superscript ± denotes the sign of the out-of-plane component, the subscript n = 1, 2, 3 labels the in-plane polarization directions [100], [010], [110], and m = 1, 2 distinguishes the two magnetic configurations, with $\mathbf{L}_2$ corresponding to the ground-state magnetic ordering. Under these conventions, we obtain four representative ferroelectric switching operations, as summarized in Fig 2d. The detailed structure mapping process including magnetic ordering is presented in Fig. S5.

$$[E||M_z]\mathbf{P}_1^+(\mathbf{L}_1) = \mathbf{P}_1^-(\mathbf{L}_1) \tag{11}$$

$$[E||M_z C_{3z}]\mathbf{P}_1^+(\mathbf{L}_1) = \mathbf{P}_2^-(\mathbf{L}_1) \tag{12}$$

$$\left[E||M_z M_y\right]\mathbf{P}_1^+(\mathbf{L}_2) = \mathbf{P}_1^-(\mathbf{L}_2) \tag{13}$$

$$\left[E||M_z M_y C_{3z}\right]\mathbf{P}_1^+(\mathbf{L}_2) = \mathbf{P}_2^-(\mathbf{L}_2) \tag{14}$$

Equations (11) and (13) correspond to ferroelectric transition path 1, while (12) and (14) correspond to path 2. Their effects on the altermagnetic spin spectrum are as follows. In Eq. (11), M_z acts in the 2D Brillouin zone as equivalent to the identity element $E \in \mathbf{H}$, realizing Type I — spin–ferroelectric decoupling. Since the M_z operation reduces to the identity in the 2D momentum space, it imposes no additional constraints and is therefore not considered further in Eqs. (12)–(14). Equation (12) involves the C_{3z} operation. Since $C_{3z} \notin \mathbf{G}$, it induces a Type III — non-symmetric mapping, geometrically rotating the momentum-space spin texture by $\pi/3$. In Eq. (13), $M_y \in A\mathbf{H}$ enacts Type II — pseudo-time-reversal coupling, producing a global reversal of spin labels. Finally, Eq. (14), the composite M_yC_{3z}, combines Type II and Type III: it applies a pseudo-time-reversal–like inversion of the spin spectrum, followed by a $\pi/3$ rotation in **k**-space. The resulting geometric and spectral reconstructions are illustrated in Fig. 3. The complete electronic structures, including the conduction bands for the $\mathbf{L}_1$ and $\mathbf{L}_2$ magnetic configurations, are presented in Fig. S6. In addition, the ferroelectric switching along path 3 exhibits a similar effect to that of path 2, as shown in Fig. S7. This result further confirms the three characteristic effects of ferroelectric switching on the spin-resolved band structure, providing a concrete material realization and a physical basis for the theoretical classification of spin-ferroelectric coupling.

Within the Boltzmann transport framework, the band structure—by governing the nonequilibrium distribution function—directly translates into electrical signals, providing a direct electrical response measurement to probe the aforementioned band mapping relationship. We accordingly calculated the spin-resolved charge conductivity σ_{yx}, as shown in Fig 4. When a current-driving electric field is applied along the mirror-symmetric *x* direction, spin-up and spin-down channels generate transverse Hall currents of opposite signs along the *y* direction. During ferroelectric switching along path 1, the spin Hall current follows the symmetry-locked characteristics of Type I or Type II coupling, either remaining unchanged in the $\mathbf{L}_1$ magnetic ordering according to Eq. (11), or reversing its overall sign in the $\mathbf{L}_2$ magnetic ordering according to Eq. (13). In contrast, along path 2, the involvement of an additional $C_{3z} \notin \mathbf{G}$ symmetry modifies the anisotropic characteristics of the spin-band, thereby giving rise to a Type III strongly

direction-asymmetric transverse current response in the $\mathbf{L}_1$ and $\mathbf{L}_2$ magnetic orderings, as described by Eq. (12) and (14). This behavior is likewise manifested during the ferroelectric transition along path 3, as shown in Fig. S8. Such distinct transport behavior provides a functional verification of the theoretical classification, clearly distinguishing the three representative coupling types identified in the symmetric analysis, and establishes an experimentally accessible electrical criterion for identifying different ferroelectric switching pathways.

3. Proof of Universality Using $BiFeO_3$ as a 3D Exemplar

To further demonstrate the generality of our symmetry-based framework beyond 2D systems, we extend our analysis to a classic 3D multiferroic material, G-type antiferromagnetic $BiFeO_3$ multiferroics with *R3c* space group, the altermagnetism was confirmed recently.[32] From a symmetry perspective, the corresponding crystallographic Laue group of this system is *3m*, and its complete set of symmetry operations is $\mathbf{G} = \{E, I, C_{3[111]}, C_{3[111]}^2, S_{3[111]}, S_{3[111]}^2, C_{2[\bar{1}10]}, C_{2[01\bar{1}]}, C_{2[10\bar{1}]}, M_{[\bar{1}10]}, M_{[01\bar{1}]}, M_{[10\bar{1}]}\}$. The halving subgroup $\mathbf{H} = \{E, I, C_{3[111]}, C_{3[111]}^2, S_{3[111]}, S_{3[111]}^2\}$ preserves each spin sublattice. Therefore, the system is described by the altermagnetic group $R_{AM} = [E||\{E, I, C_{3[111]}, C_{3[111]}^2, S_{3[111]}, S_{3[111]}^2\}] + [C_2||\{C_{2[\bar{1}10]}, C_{2[01\bar{1}]}, C_{2[10\bar{1}]}, M_{[\bar{1}10]}, M_{[01\bar{1}]}, M_{[10\bar{1}]}\}]$, representing a *g*-wave altermagnetic system, as shown in Fig. 5a-b.

In bulk $BiFeO_3$, the *R3c* crystal structure arises from $Pm\bar{3}m$ by the condensation of two primary order parameters: a polar distortion along the [111] direction and a rotation of the oxygen octahedra along the [111] direction, described by the R_4^+ irreducible representation. For polarization switching achieved by independent displacement of Bi^{3+} ions (referred to as path 1), the overall effect is equivalent to an inversion operation $O_{FE} = I$, i.e., $[E||I]\mathbf{P} = \mathbf{P'}$ (Fig. 5b). However, in certain conditions, polarization switching may be accompanied by the rotation of the oxygen octahedra (referred to as path 2).[34] In this case, inversion symmetry cannot map the lattice structure while preserving the system's magnetic ordering; instead, path 2 affects the system in an $O_{FE} = C_{2[\bar{1}10]}$ manner, i.e., $[E||C_{2[\bar{1}10]}]\mathbf{P} = \mathbf{P'}$ (Fig. 5b). According to Eq. 9, the path 1, where O_{FE}

$\in \mathbf{H}$, does not alter the spin splitting during polarization reversal, and is classified as Type I (decoupled). The path 2, where $O_{FE} \in A\mathbf{H}$, maps the opposite spin channels and is classified as Type II (pseudo-time-reversal coupling). The band structure calculations shown in Fig. 5 clearly confirm these two distinct responses.

This analysis not only emphasizes that the spin splitting control in $BiFeO_3$ is directly related to octahedral rotation rather than polarization switching, providing an intuitive symmetry perspective for electric control of spin splitting in $BiFeO_3$, but also clarifies the universal applicability of this symmetry mechanism in various multiferroic materials. By identifying the symmetry of the ferroelectric switching operation, one can predict and classify its magnetoelectric coupling functionality, independent of the specific system under study.

III. DISCUSSION

In summary, we have established a unified symmetry-based framework that classifies magnetoelectric coupling in altermagnetic multiferroics. Using the spin Laue group formalism, we identify three fundamental types of spin–ferroelectric coupling, governed entirely by the relation between the ferroelectric switching operator and the underlying magnetic symmetry. These theoretical predictions are corroborated by first-principles calculations on bilayer $MnPS_3$ and $BiFeO_3$, demonstrating that distinct ferroelectric switching paths indeed produce characteristic spin-band reconstructions. Crucially, each coupling type yields distinct electrical transport signatures—particularly in the spin Hall response—thereby directly linking abstract symmetry principles to tangible, experimentally observable effects. This framework not only provides a practical blueprint for designing altermagnetic multiferroics with tailored magnetoelectric functionality but also establishes a general approach for exploring spin-ferroelectric coupling, paving the way for voltage-controlled, low-power spintronic applications.

IV. METHODS

The atomic properties and electronic structure of the materials were calculated using first-

principles simulations within density functional theory (DFT)[35,36]. The projected augmented wave pseudopotentials method, as implemented in the Vienna *Ab* initio Simulation Package (VASP)[37,38] was employed. The exchange-correlation energy was calculated using the generalized gradient approximation (GGA) of the Perdew-Burke-Ernzerhof form[39], and the plane wave cutoff energy was set to 500 eV. A Hubbard U_{eff} = 4 eV with the Dudarev parametrization was applied to properly describe the localization of Mn 3*d* orbitals.[40] The semiempirical DFT-D3 method was used to include the van der Waals interaction[41]. For $MnPS_3$ calculations, a centered 9 × 9 × 1 Monkhorst-Pack *k*-point mesh was used.[42] To eliminate periodic boundary effects, the vacuum space between adjacent slabs was set to exceed 15 Å along the *z* direction. Using the conjugate gradient method, the plane lattice constant and atomic coordinates were fully relaxed until the energy and force converged to 10^{-6} and 10^{-2} eV/Å, respectively. The Berry-phase method was employed to evaluate polarization magnitude,[43] and the ferroelectric transition switching pathway was obtained using the climbing image nudged elastic band (CI-NEB) method.[44] The spin-resolved charge conductivity was calculated using Boltzmann transport theory within the constant-relaxation-time approximation as implemented in Wannier90 package,[45] with the electronic temperature and relaxation time set to 300 K and 1 ps, respectively. The lattice structure was visualized using VESTA.[46]

Data Availability

Relevant data generated in this study are provided in the article and Supplementary Information.

References

1 Duan, X., Zhang, J., Zhu, Z., Liu, Y., Zhang, Z., Žutić, I. & Zhou, T. Antiferroelectric altermagnets: Antiferroelectricity alters magnets. *Physical review letters* **134**, 106801 (2025).
2 Gu, M., Liu, Y., Zhu, H., Yananose, K., Chen, X., Hu, Y., Stroppa, A. & Liu, Q. Ferroelectric switchable altermagnetism. *Physical review letters* **134**, 106802 (2025).
3 Sun, W., Yang, C., Wang, W., Liu, Y., Wang, X., Huang, S. & Cheng, Z. Proposing

Altermagnetic-Ferroelectric Type-III Multiferroics with Robust Magnetoelectric Coupling. *Advanced Materials*, 2502575 (2025).

4 Sun, W., Wang, W., Yang, C., Hu, R., Yan, S., Huang, S. & Cheng, Z. Altermagnetism induced by sliding ferroelectricity via lattice symmetry-mediated magnetoelectric coupling. *Nano Letters* **24**, 11179-11186 (2024).

5 Fiebig, M., Lottermoser, T., Meier, D. & Trassin, M. The evolution of multiferroics. *Nature Reviews Materials* **1**, 16046 (2016).

6 Dong, S., Xiang, H. & Dagotto, E. Magnetoelectricity in multiferroics: a theoretical perspective. *National Science Review* **6**, 629-641 (2019).

7 Šmejkal, L., Sinova, J. & Jungwirth, T. Beyond conventional ferromagnetism and antiferromagnetism: A phase with nonrelativistic spin and crystal rotation symmetry. *Physical Review X* **12**, 031042 (2022).

8 Fedchenko, O., Minár, J., Akashdeep, A., D'Souza, S. W., Vasilyev, D., Tkach, O., Odenbreit, L., Nguyen, Q., Kutnyakhov, D. & Wind, N. Observation of time-reversal symmetry breaking in the band structure of altermagnetic RuO_2. *Science Advances* **10**, eadj4883 (2024).

9 Krempaský, J., Šmejkal, L., D'souza, S., Hajlaoui, M., Springholz, G., Uhlířová, K., Alarab, F., Constantinou, P., Strocov, V. & Usanov, D. Altermagnetic lifting of Kramers spin degeneracy. *Nature* **626**, 517-522 (2024).

10 Reimers, S., Odenbreit, L., Šmejkal, L., Strocov, V. N., Constantinou, P., Hellenes, A. B., Jaeschke Ubiergo, R., Campos, W. H., Bharadwaj, V. K. & Chakraborty, A. Direct observation of altermagnetic band splitting in CrSb thin films. *Nature Communications* **15**, 2116 (2024).

11 McClarty, P. A. & Rau, J. G. Landau theory of altermagnetism. *Physical review letters* **132**, 176702 (2024).

12 Lee, S., Lee, S., Jung, S., Jung, J., Kim, D., Lee, Y., Seok, B., Kim, J., Park, B. G. & Šmejkal, L. Broken kramers degeneracy in altermagnetic MnTe. *Physical review letters* **132**, 036702 (2024).

13 Cao, R., Dong, R., Fei, R. & Yao, Y. Designing Spin-driven Multiferroics in Altermagnets. *arXiv preprint arXiv:2412.20347* (2024).

14 Mazin, I., González-Hernández, R. & Šmejkal, L. Induced Monolayer Altermagnetism in $MnP(S, Se)_3$ and FeSe. *arXiv preprint arXiv:2309.02355* (2023).

15 Brekke, B., Brataas, A. & Sudbø, A. Two-dimensional altermagnets: Superconductivity in a minimal microscopic model. *Physical Review B* **108**, 224421 (2023).

16 Šmejkal, L., Sinova, J. & Jungwirth, T. Emerging Research Landscape of Altermagnetism. *Physical Review X* **12**, 040501 (2022).

17 Bai, L., Feng, W., Liu, S., Šmejkal, L., Mokrousov, Y. & Yao, Y. Altermagnetism: Exploring new frontiers in magnetism and spintronics. *Advanced Functional Materials* **34**, 2409327 (2024).

18 Song, C., Bai, H., Zhou, Z., Han, L., Reichlova, H., Dil, J. H., Liu, J., Chen, X. & Pan, F. Altermagnets as a new class of functional materials. *Nature Reviews Materials* **10**, 473–485 (2025).

19 Wei, C.-C., Lawrence, E., Tran, A. & Ji, H. Crystal Chemistry and Design Principles of

Altermagnets. *ACS Organic & Inorganic Au* **4**, 604-619 (2024).

20 Ma, H.-Y., Hu, M., Li, N., Liu, J., Yao, W., Jia, J.-F. & Liu, J. Multifunctional antiferromagnetic materials with giant piezomagnetism and noncollinear spin current. *Nature communications* **12**, 2846 (2021).

21 Wu, Y., Deng, L., Yin, X., Tong, J., Tian, F. & Zhang, X. Valley-related multipiezo effect and noncollinear spin current in an altermagnet Fe2Se2O monolayer. *Nano Letters* **24**, 10534-10539 (2024).

22 Liu, C., Li, X., Li, X. & Yang, J. Realizing Abundant Two-Dimensional Altermagnets with Anisotropic Spin Current Via Spatial Inversion Symmetry Breaking. *Nano Letters* (2025).

23 Sheoran, S. & Dev, P. Spontaneous anomalous Hall effect in two-dimensional altermagnets. *Physical Review B* **111**, 184407 (2025).

24 Šmejkal, L., González-Hernández, R., Jungwirth, T. & Sinova, J. Crystal time-reversal symmetry breaking and spontaneous Hall effect in collinear antiferromagnets. *Science advances* **6**, eaaz8809 (2020).

25 Šmejkal, L., MacDonald, A. H., Sinova, J., Nakatsuji, S. & Jungwirth, T. Anomalous hall antiferromagnets. *Nature Reviews Materials* **7**, 482-496 (2022).

26 Zhou, X., Feng, W., Yang, X., Guo, G.-Y. & Yao, Y. Crystal chirality magneto-optical effects in collinear antiferromagnets. *Physical Review B* **104**, 024401 (2021).

27 Feng, Z., Zhou, X., Šmejkal, L., Wu, L., Zhu, Z., Guo, H., González-Hernández, R., Wang, X., Yan, H. & Qin, P. An anomalous Hall effect in altermagnetic ruthenium dioxide. *Nature Electronics* **5**, 735-743 (2022).

28 Šmejkal, L. Altermagnetic multiferroics and altermagnetoelectric effect. *arXiv preprint arXiv:2411.19928* (2024).

29 Zhu, Y., Gu, M., Liu, Y., Chen, X., Li, Y., Du, S. & Liu, Q. Sliding ferroelectric control of unconventional magnetism in stacked bilayers. *Physical review letters* **135**, 056801 (2025).

30 Zhu, Z., Duan, X., Zhang, J., Hao, B., Zutic, I. & Zhou, T. Two-dimensional ferroelectric altermagnets: From model to material realization. *Nano Letters* (2025).

31 Sun, W., Wang, W., Yang, C., Huang, S., Ding, N., Dong, S. & Cheng, Z. Designing Spin Symmetry for Altermagnetism with Strong Magnetoelectric Coupling. *Advanced Science*, e03235 (2025).

32 Urru, A., Seleznev, D., Teng, Y., Park, S. Y., Reyes-Lillo, S. E. & Rabe, K. M. G-type antiferromagnetic $BiFeO_3$ is a multiferroic *g*-wave altermagnet. *Physical Review B* **112**, 104411 (2025).

33 Ji, J., Yu, G., Xu, C. & Xiang, H. General Theory for Bilayer Stacking Ferroelectricity. *Physical review letters* **130**, 146801 (2023).

34 Heron, J., Bosse, J., He, Q., Gao, Y., Trassin, M., Ye, L., Clarkson, J., Wang, C., Liu, J. & Salahuddin, S. Deterministic switching of ferromagnetism at room temperature using an electric field. *Nature* **516**, 370-373 (2014).

35 Kohn, W. & Sham, L. J. Self-consistent equations including exchange and correlation effects. *Physical Review* **140**, A1133 (1965).

36 Hohenberg, P. & Kohn, W. Inhomogeneous electron gas. *Physical Review* **136**, B864 (1964).

37 Kresse, G. & Hafner, J. Ab initio molecular dynamics for liquid metals. *Physical review B* **47**, 558 (1993).
38 Kresse, G. & Furthmüller, J. Efficient iterative schemes for ab initio total-energy calculations using a plane-wave basis set. *Physical review B* **54**, 11169 (1996).
39 Perdew, J. P., Burke, K. & Ernzerhof, M. Generalized gradient approximation made simple. *Physical review letters* **77**, 3865 (1996).
40 Dudarev, S. L., Botton, G. A., Savrasov, S. Y., Humphreys, C. & Sutton, A. P. Electron-energy-loss spectra and the structural stability of nickel oxide: An LSDA+ U study. *Physical Review B* **57**, 1505 (1998).
41 Grimme, S., Antony, J., Ehrlich, S. & Krieg, H. A consistent and accurate ab initio parametrization of density functional dispersion correction (DFT-D) for the 94 elements H-Pu. *The Journal of Chemical Physics* **132**, 154104 (2010).
42 Monkhorst, H. J. & Pack, J. D. Special points for Brillouin-zone integrations. *Physical review B* **13**, 5188 (1976).
43 King-Smith, R. & Vanderbilt, D. Theory of polarization of crystalline solids. *Physical Review B* **47**, 1651 (1993).
44 Henkelman, G. & Jónsson, H. Improved tangent estimate in the nudged elastic band method for finding minimum energy paths and saddle points. *The Journal of chemical physics* **113**, 9978-9985 (2000).
45 Pizzi, G., Vitale, V., Arita, R., Blügel, S., Freimuth, F., Géranton, G., Gibertini, M., Gresch, D., Johnson, C. & Koretsune, T. Wannier90 as a community code: new features and applications. *Journal of Physics: Condensed Matter* **32**, 165902 (2020).
46 Momma, K. & Izumi, F. VESTA 3 for three-dimensional visualization of crystal, volumetric and morphology data. *Applied Crystallography* **44**, 1272-1276 (2011).

Acknowledgements

W.S. acknowledges the support from the National Natural Science Foundation of China (Grant No. 12304141) and the Shandong Provincial Natural Science Foundation (Grant No. ZR2023QA001), W.S. and S.F.H. are grateful for the Taishan Scholars Program (Grants No. tsqn202312209 and No. tstp20221130), W.X.W. thanks the China Postdoctoral Science Foundation (Grant No. 2025M783391), S.F.H. acknowledges the Shandong provincial key research and development plan (Grant No. 2022CXPT045) and the 111 Project of International Corporation on Advanced Cement-based Materials (No. D17001). Z.X.C. thanks Australia Research Council for support (DP260102992).

Author contributions

The conceptualization was carried out by W.S. and Z.X.C. Data curation was performed by W.S. and W.X.W. The visualization and original draft were completed by W.S. Formal analysis, as well as reviewing and editing the manuscript, was conducted by Z.X.C. Funding was acquired by W.S., W.X.W., S.F.H., and Z.X.C. Supervision and validation were handled by C.H.Y.

Competing interests

The authors declare no competing interests.

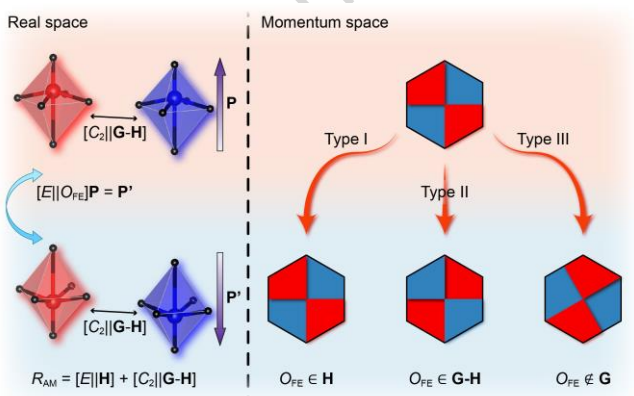

Fig. 1. Three fundamental types of spin-ferroelectric coupling in altermagnetic multiferroics. Type I corresponding to spin–ferroelectric decoupling, Type II to pseudo-time-reversal coupling, and Type III to non-symmetric momentum mapping. Red and blue represent opposite spin orientations. While the real-space spins configuration remains invariant under ferroelectric switching, the momentum-space spin texture shows distinctly different reconstruction for each type.

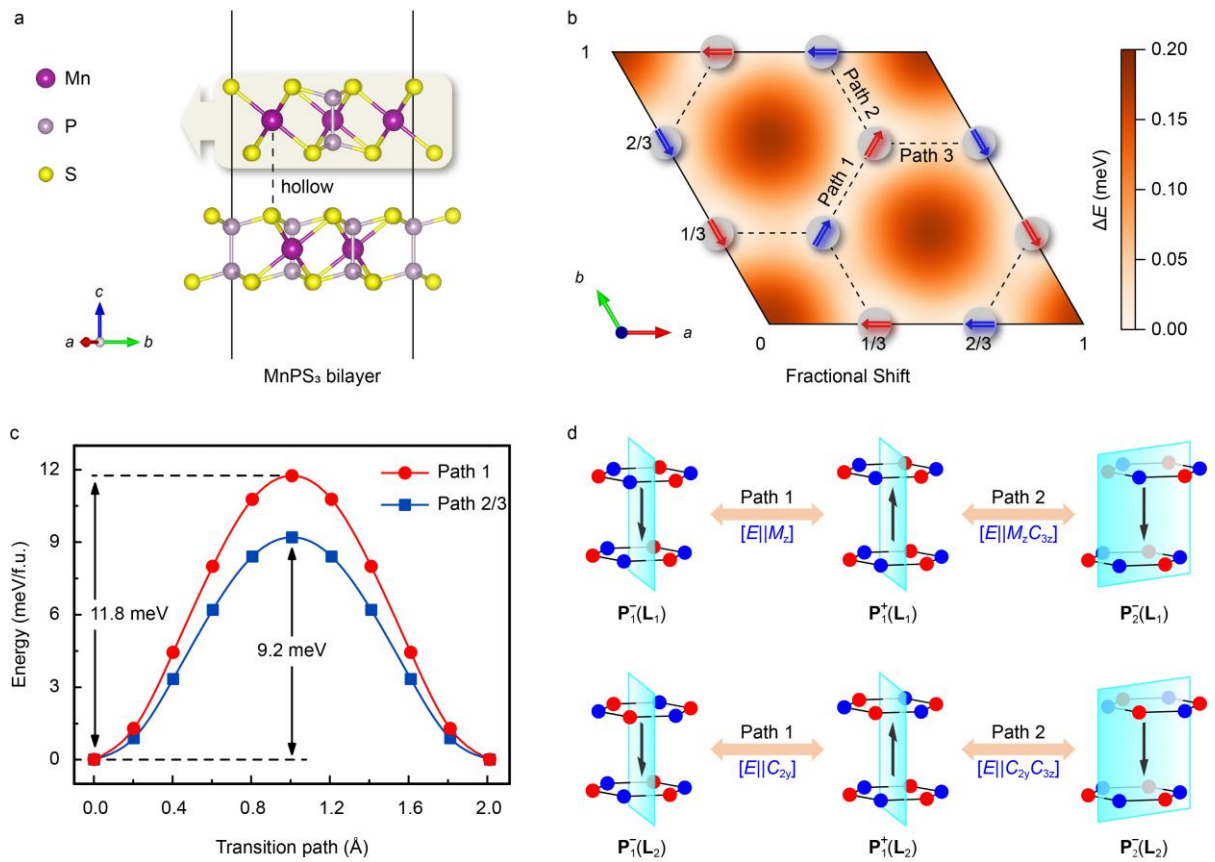

Fig. 2. Schematic of the bilayer $MnPS_3$ structure and ferroelectric switching. (a) Bilayer $MnPS_3$ constructed by applying the symmetry operations $\{M_z|\tau_o\}$ and out-of-plane translation τ_z to a monolayer, exhibiting the crystallographic Laue group *2/m*. (b) Energy distribution as a function of in-plane translations τ_o, with arrows denoting in-plane polarization directions at the six degenerate global minima. Red and blue arrows indicate opposite out-of-plane components. Dashed lines mark the ferroelectric transition paths, with (c) showing the corresponding energy barriers. (d) Ferroelectric switching symmetry operations under different magnetic orders ($\mathbf{L}_1/\mathbf{L}_2$) and transition paths (path 1/path 2). The cyan plane represents the crystal mirror plane, aligned with the in-plane polarization, while black arrows depict the out-of-plane polarization component, and red and blue represent opposite spin sublattices.

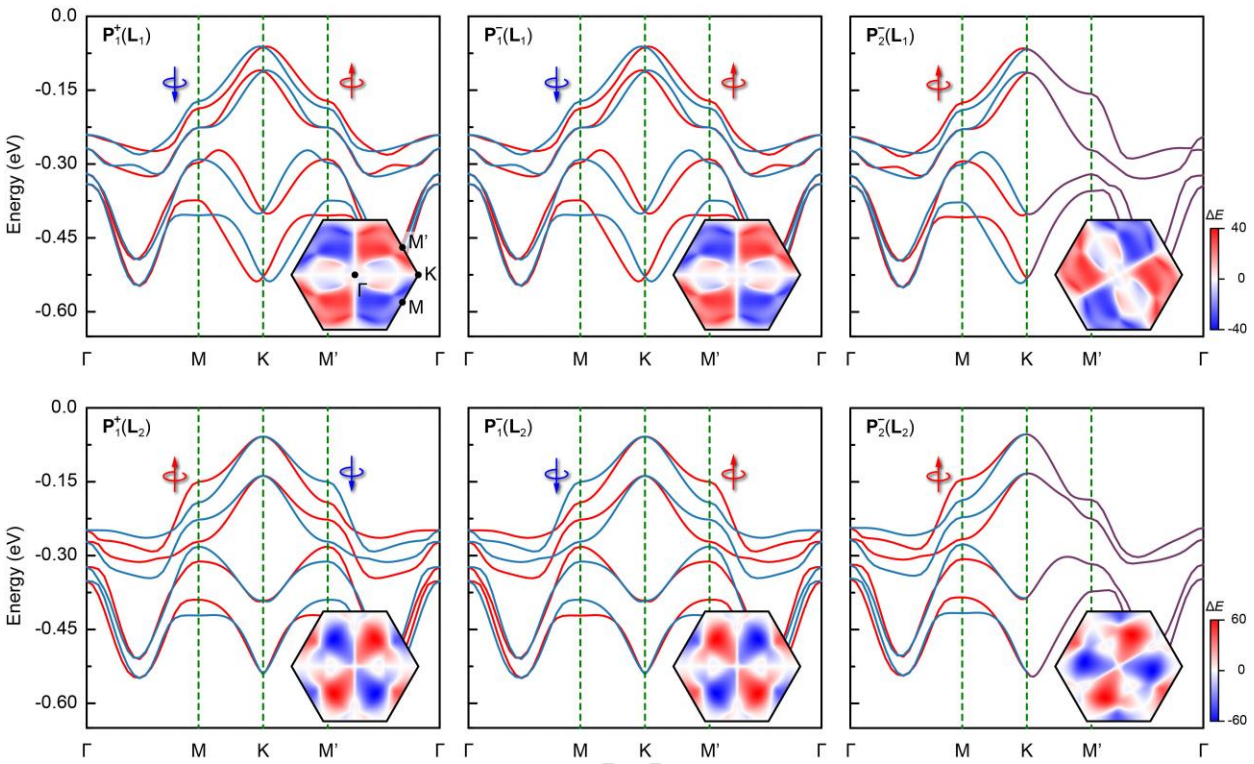

Fig. 3. Band structures under different magnetic orderings and polarization configurations. The spin-splitting energy on the valence band maximum across the first Brillouin zone is described by the insets. Red and blue represent opposite spin orientations. For transition path 1 between $\mathbf{P}_1^+$ and $\mathbf{P}_1^-$, the spin spectrum either remains unchanged ($\mathbf{L}_1$) or exhibits a global reversal ($\mathbf{L}_2$). In contrast, path 2 between $\mathbf{P}_1^+$ and $\mathbf{P}_2^-$ introduce an additional C_{3z} geometric mapping to the spin spectrum.

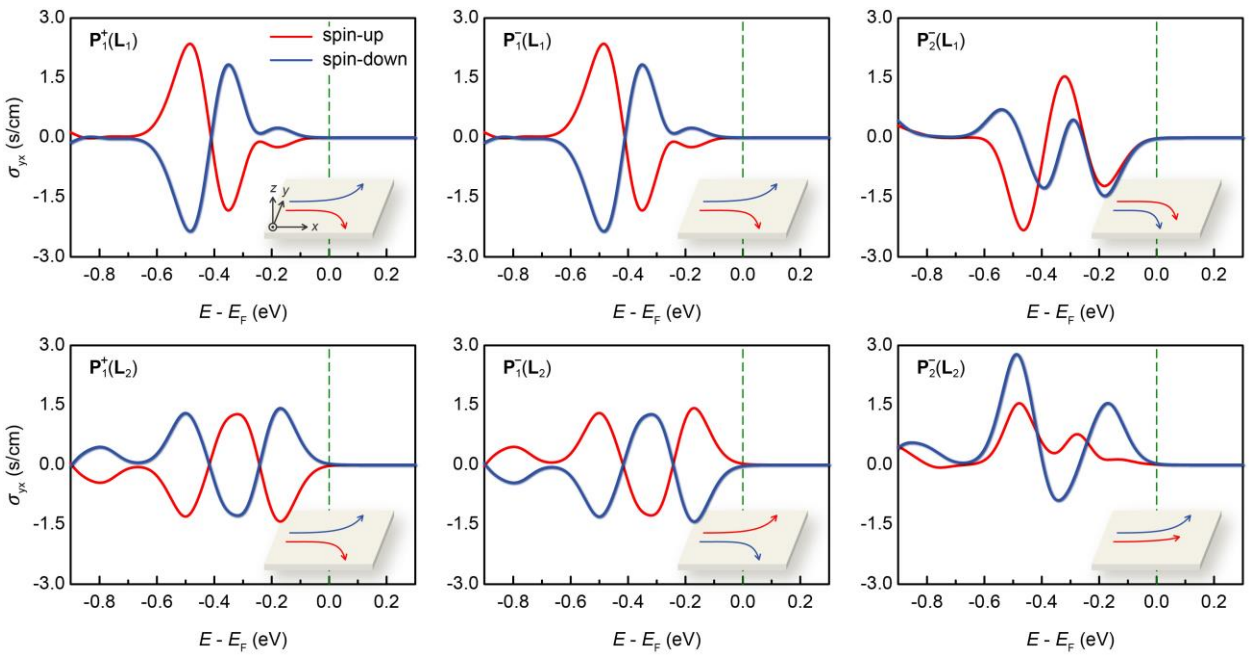

Fig. 4. Spin-resolved charge conductivity under different magnetic orderings and polarization configurations. The green dashed line indicates the Fermi level, with the inset showing the transport response at -0.1 eV. For the $\mathbf{P}_1^{\pm}$ states, opposite spin channels exhibit conductivities of opposite signs, with the direction determined by the type I or type II spin–ferroelectric coupling. In contrast, the transition from the $\mathbf{P}_1^{+}$ to $\mathbf{P}_2^{-}$ states display an anisotropic modification that disrupts this spin-dependent signature and generate an asymmetric transverse spin current.

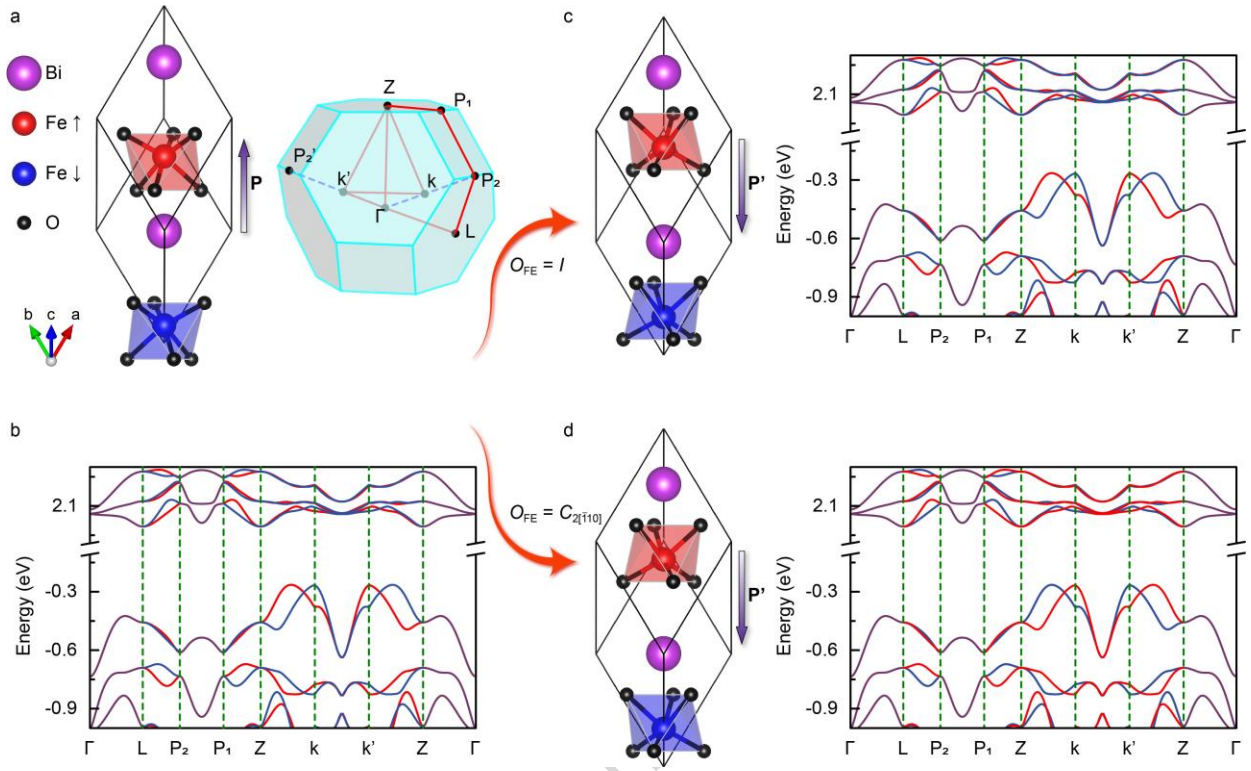

Fig. 5. Spin band structure corresponds to ferroelectric switching in $BiFeO_3$ multiferroics. (a) The crystal structure of $BiFeO_3$ and its corresponding Brillouin zone of the rhombohedral lattice. Red and blue represent Fe ions with opposite spins, with k (k') located at the midpoint between Γ and P_2 (P_2') in the Brillouin zone. (b) Spin-splitting band structure with altermagnetism. (c) and (d) represent two ferroelectric switching paths, where the spin band structure remains unchanged under $O_{FE} = I$, but reverses under $O_{FE} = C_{2[\bar{1}10]}$.

Editor's summary:

The authors establish a universal symmetry framework that classifies spin–ferroelectric couplings in altermagnetic multiferroics into three fundamental types: decoupling, pseudo-time-reversal coupling, and asymmetric momentum mapping.

Peer review information: *Nature Communications* thanks the anonymous reviewer(s) for their contribution to the peer review of this work. A peer review file is available.